nature physics

LETTERS

https://doi.org/10.1038/s41567-019-0537-1

Quantum simulation of Unruh radiation

Jiazhong Hu*, Lei Feng, Zhendong Zhang and Cheng Chin

The exploration of quantum phenomena in a curved spacetime is an emerging interdisciplinary area at the interface between general relativity[1-4], thermodynamics[4-6] and quantum information[7,8]. One famous prediction in this field is Unruh thermal radiation[3]—the manifestation of thermal radiation from a Minkowski vacuum when viewed in an accelerating reference frame. Here, we report the experimental observation of a matter field with thermal fluctuations that agree with Unruh's predictions. The matter field is generated within a framework for the simulation of quantum physics in a non-inertial frame, based on Bose–Einstein condensates that are parametrically modulated[9] to make their evolution replicate the frame transformation. We further observe long-range phase coherence and temporal reversal of the matter-wave radiation, hallmarks that distinguish Unruh radiation from its classical counterpart. Our demonstration offers a new avenue for the investigation of the dynamics of quantum many-body systems in a curved spacetime.

Applying quantum mechanics to gravitational systems or curved spacetimes is one exciting area in the exploration of the not-yet-understood physics of quantum gravity. Ideas such as Hawking radiation[1,2], gauge–gravity duality[10] and the black hole information paradox[11–13] improve our understanding of quantum mechanics in gravitational fields, and are essential steps toward a new approach to the foundations of physics.

Here we propose a new method to study quantum systems in curved spacetimes on the basis of simulation of quantum systems in an accelerating frame; the notion originates from the equivalence principle that physics in a gravitational field cannot be distinguished from that in an accelerating frame on the basis of local measurements. Specifically, we demonstrate the Rindler frame transformation $\hat{R}_A$ (refs. [4,14]) with acceleration A by evolving the system with the pair-creation Hamiltonian $\hat{\mathcal{H}}$. Given a quantum state Ψ_0, our method can be understood as the equivalence of the time evolution $\hat{U}(\tau)=\exp(-i\hat{\mathcal{H}}\tau/\hbar)$ and the Rindler transformation $\hat{R}_A$, namely

$$\hat{U}(\tau)\Psi_0=\hat{R}_A\Psi_0 \tag{1}$$

where $2\pi\hbar$ is the Planck constant and τ is the evolution time. With this method, we can simulate physics in a highly accelerating frame based on a bench-top experiment without physically accelerating the sample.

When the quantum system is a vacuum in the Minkowski space, it is predicted that an accelerating observer will detect a thermal radiation from the system (Unruh effect)[3]. The thermal radiation is characterized by the Unruh temperature

$$T_U=\frac{\hbar A}{2\pi c k_B} \tag{2}$$

where k_B is the Boltzmann constant and c is the speed of light. Because of the equivalence principle, this surprising phenomenon shares the same root as Hawking radiation[2,3]. It is, however, extremely challenging to observe the Unruh effect experimentally; an enormous acceleration of $A=2.5\times10^{14}\,\mathrm{m\,s^{-2}}$ is required to generate Unruh radiation of merely $T_U=1\,\mu\mathrm{K}$.

To generate the frame boost for any quantum state ψ_0, we find that the required Hamiltonian $\mathcal{H}=i\hbar\sum_k g_k(a_k^\dagger a_{-k}^\dagger-a_k a_{-k})$ describes the pair creation of excitations with opposite momenta. Here a_k and $a_k^\dagger$ are the annihilation and creation operators with wavenumber k and g_k is the coupling constant. The acceleration of the frame transformation is given by (Methods)

$$A=\frac{\pi E_k c}{2\hbar\ln\coth(g_k\tau)} \tag{3}$$

where E_k is the energy of the excitation. Combining equations (2) and (3), we see that the Unruh temperature scale is given by the excitation energy as $k_B T_U=E_k/[4\ln\coth(g_k\tau)]$.

In this paper, we demonstrate the above idea and simulate the Unruh effect by only considering the momentum modes with the same amplitude $|\mathbf{k}|=k_f$ (see Fig. 1). By modulating the interactions of a Bose condensate with frequency ω, we prepare the pair-creation Hamiltonian. Under the Bogoliubov and the rotating wave approximations (Methods), the Hamiltonian reduces to

$$H=i\hbar g\sum_{|\mathbf{k}|=k_f}(a_k^\dagger a_{-k}^\dagger-a_k a_{-k}) \tag{4}$$

where $k_f=\sqrt{m\omega/\hbar}$ and m is the atomic mass. Given the modulation, the condensate in our experiment radiates atoms into about 300 momentum modes, sufficient to test the predicted thermal fluctuations $P(n)\propto e^{-nE/k_BT}$, where n is the atom number and $E=\hbar\omega/2$ is the energy of an emitted atom. We observe excellent agreement with thermal models and Unruh's predictions. We further show the non-local spatial coherence and reversibility of the matter-wave generation, which clearly distinguish the Unruh radiation from its classical counterpart (black-body radiation), and confirm the quantum nature of matter-wave generation.

Our experiment starts with a Bose–Einstein condensate of 60,000 caesium atoms confined in a disc-shaped optical dipole trap. By modulating the magnetic field at a frequency near a Feshbach resonance[15,16], a two-dimensional, jet-like emission of atoms with momentum $|k|=k_f$ is observed on the basis of in situ imaging after a few milliseconds (see Methods for experimental details). This emission forms a fluctuating bosonic field, also called 'Bose fireworks', and is a result of stimulated amplification of quantum fluctuations[9,17]. Its evolution can be well described by the Hamiltonian in equation (4).

James Franck Institute, Enrico Fermi Institute and Department of Physics, University of Chicago, Chicago, IL, USA. *e-mail: hujiazhong01@ultracold.cn

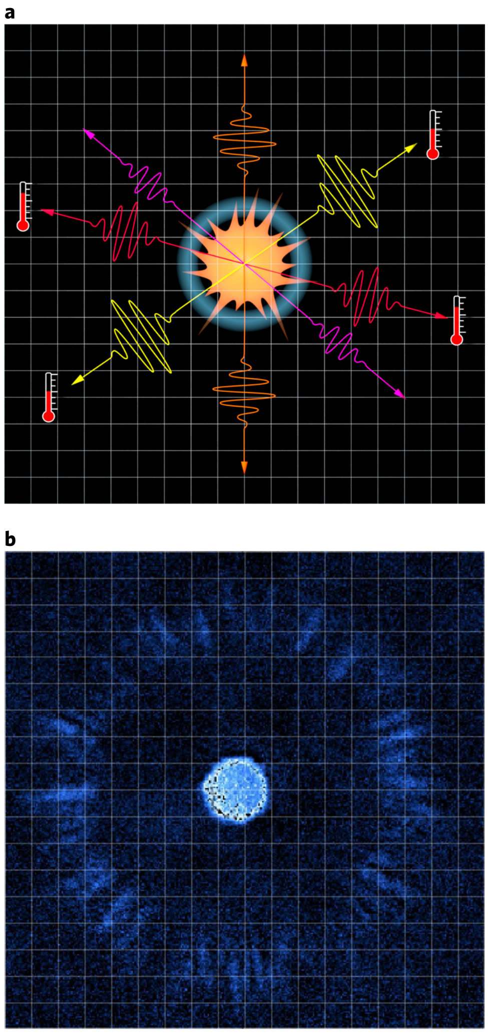

Fig. 1 | Quantum simulation of Unruh radiation. a, To an observer in an accelerating frame, a vacuum state in the inertial frame appears identical to a thermal state with the Unruh temperature T_U. **b**, We simulate the Unruh radiation by parametrically modulating the interactions of an atomic condensate, whose evolution is equivalent to a coordinate transformation to an accelerating frame without actually accelerating the system. The matter-wave field shares the same characteristics as the Unruh radiation: it is locally indistinguishable from a Boltzmann distribution, but is long-range coherent and temporally reversible.

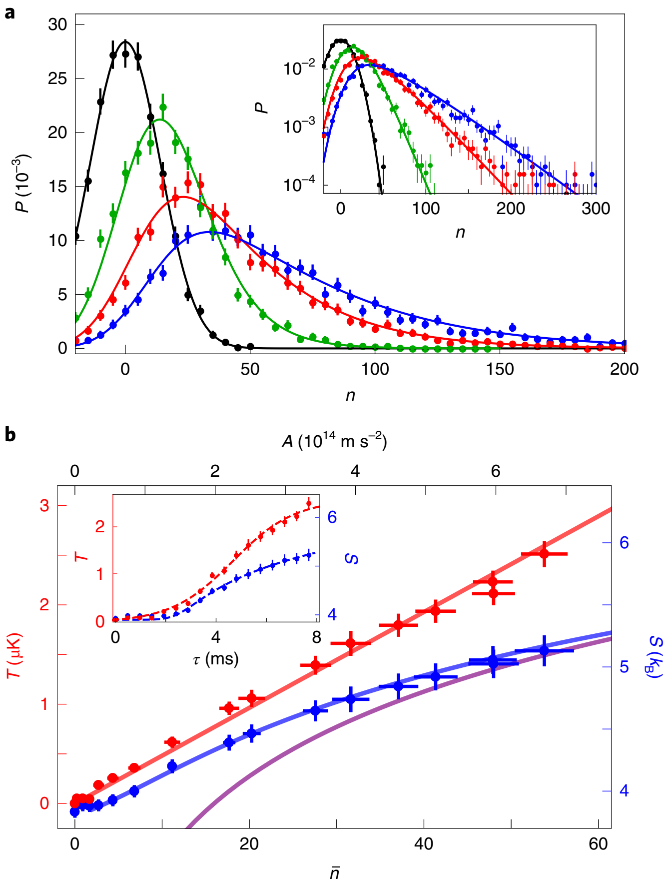

Fig. 2 | Thermal behaviour of the matter-wave emission. a, The measured probability $P(n)$ of n atoms within a 2° slice of the emission pattern after evolution time $\tau = 0$, 3.36, 4.8 and 6.24 ms (black, green, red and blue circles). The solid lines are fits based on a thermal model (Methods). The inset shows the data in a log scale. **b**, Temperature T and entropy S versus the mean population per mode $\bar{n}$. The derived acceleration A is shown at the top. The red solid line is a fit of $T = \kappa A/c$. The blue solid line is the prediction that includes the detection noise and the purple line is the prediction excluding the noise. The inset shows the evolution of T and S. The dashed lines are guides to the eye. Here the condensate's radius is 13 μm. The scattering length is modulated at frequency $\omega/2\pi = 2.1$ kHz with a small offset of $a_{dc} = 4\,a_0$ and an amplitude of $a_{ac} = 50\,a_0$, where a_0 is the Bohr radius. All error bars correspond to 1 s.d. of the mean values.

In typical experiments, the emission carries as many as 276 angular modes and each mode acquires a width of 1.30° (Methods). To study the distribution of the mode population, we divide the emission pattern evenly into 180 angular slices. For each slice, we extract n and evaluate the probability distribution of the mode population $P(n)$ (see Fig. 2a).

The measured mode population distributions strongly resemble that from thermal radiation (see Fig. 2a). We extract the effective temperature T on the basis of a thermal model, which incorporates both the Boltzmann distribution and the measurement uncertainty (Methods). The model fits the data excellently, and the extracted temperature shows a linear dependence on the mean atomic population per mode $\bar{n} = (1/\xi)\int nP(n)\,\mathrm{d}n$ with $\xi = 2°/1.30° = 1.5$ the average number of modes within a 2° slice (Fig. 2b). Such linear mapping between temperature and mean population is consistent with the thermodynamic calculation, which yields $k_B T \approx E\bar{n}$ (Methods).

The thermal distribution of the mode population can be understood in terms of the Unruh effect. The matter-wave field measured in our system simulates the vacuum state observed in an accelerating frame. We evaluate A (Fig. 2b), from which we observe a linear relation between the temperature and the acceleration, $T = \kappa A/c$. By fitting the data, we obtain the ratio $\kappa = 1.17(7)$ pK s. Our result agrees well with the Unruh prediction $\kappa = \hbar/2\pi k_B \approx 1.22$ pK s (equation (2)).

In addition to the temperature, we further evaluate the mean entropy of a single momentum mode $S = -k_B\sum_n P(n)\ln P(n) - S_0$, an important observable to characterize the matter-wave radiation (Methods). For short $\tau < 3$ ms, the measured entropy is dominated by the detection noise $S_b = 3.8\,k_B$. For long modulations, the measurement faithfully reflects the entropy of the matter-wave radiation. The entropy increases logarithmically with A (Fig. 2b), and agrees with the calculation $S \approx k_B\ln(e\bar{n})$ (Methods). The entropy measurement again confirms that the emission forms a thermal field.

While local measurements in our system seem to reveal a thermal distribution, unlike incoherent black-body radiation, Unruh

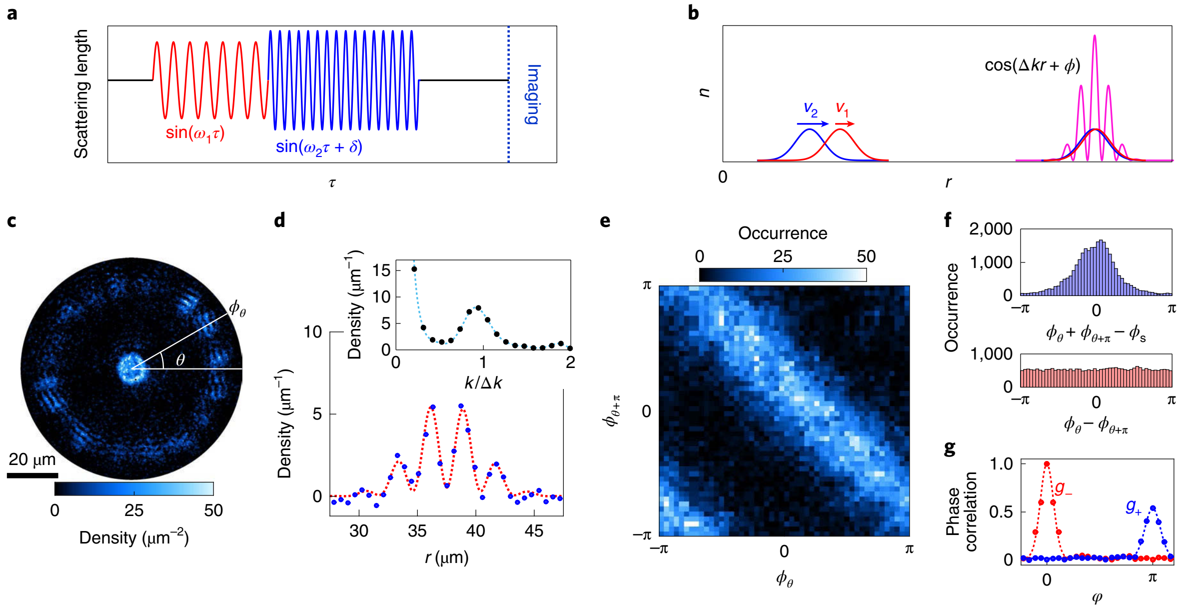

Fig. 3 | Long-range phase correlation of matter-wave radiation. Here the condensates are confined in a disc-shaped trap with radius 7 μm. **a**, Application of two pulses of scattering length modulation with frequencies $\omega_1/2\pi = 3$ and $\omega_2/2\pi = 5.63$ kHz, and $a_{\mathrm{ac}} = 56$ and 72 a_0. The relative phase of the pulses is δ. **b**, The matter-wave jet created by the latter pulse propagates at a greater speed $v_2 > v_1$ and interferes with atoms from the first pulse when they overlap. Here the matter-wave speeds are $v_i = \sqrt{\hbar\omega_i/m}$ for the ith pulse. The interference is characterized by the wavenumber difference $\Delta k = k_2 - k_1$, relative phase ϕ and radial distance r. **c**, An example interference pattern of the two radiation fields. The phase of the interference fringes ϕ_θ is recorded as a function of θ. **d**, A radial cut of the interference pattern, from which we determine the phase of the fringes on the basis of Fourier transformation (Methods). Dotted lines are guides to the eye. **e**,**f**, The concurrence of the extracted phases in the opposite directions, ϕ_θ and $\phi_{\theta+\pi}$, for all θ from a collection of 200 images. A strong correlation of the two phases is described by $\phi_\theta + \phi_{\theta+\pi} = \phi_s$, where $\phi_s = 0.79(3)$ is obtained from fitting the data; $\phi_\theta - \phi_{\theta+\pi}$ appears to be random. **g**, Phase correlations g_+ and g_- between fringes separated by an angular distance φ (equation (5)). Points represent experimental data while dashed curves are guides to the eye (Methods).

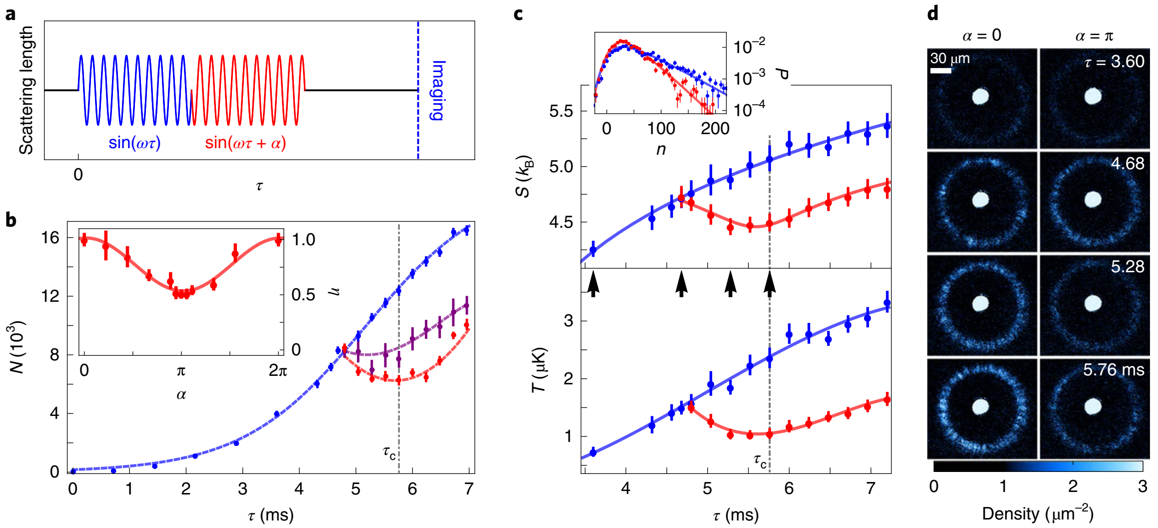

Fig. 4 | Time reversal of the matter-wave radiation field. a, The scattering length is modulated at $\omega/2\pi = 2.1$ kHz with $a_{\mathrm{ac}} = 50\,a_0$ for time $\tau = 4.75$ ms before a phase jump α is introduced to the modulation. **b**, Emitted atom number N versus time τ. The blue, purple and red data correspond to $\alpha = 0$, $2\pi/3$ and π, respectively. The dashed lines are guides to the eye. The inset shows suppression ratio η versus phase jump α evaluated at $\tau = \tau_c$. A sinusoidal fit gives the maximum reversal at $\alpha = 0.98(3)\pi$, where η reaches 51(3)%. **c**, Entropy S and temperature T without ($\alpha = 0$, blue circles) and with the phase jump ($\alpha = \pi$, red circles). The lines here are guides to the eye. The inset compares $P(n)$ at τ_c with $\alpha = 0$ (blue) and π (red). The solid lines are the fits from our thermal model. **d**, The average of 15 images of the matter-wave radiation at different times (indicated by arrows in **c**) with $\alpha = 0$ or π. Here the condensates are confined in a disc-shaped trap with radius 13 μm. All error bars correspond to 1 s.d. of the mean value.

radiation should exhibit both spatial and temporal coherence, reflecting its quantum origin. In the following we investigate the coherence properties of the matter-wave radiation.

We first show the spatial coherence of the matter-wave field by probing the phase correlation between jets. To do this, we perform a matter-wave interference experiment by applying two independent pulses of modulation on the scattering length; the first pulse has a lower frequency than the second one (Fig. 3a). The two frequencies are incommensurate to avoid influence from high-harmonic generation[17]. The pulses are arranged such that the atoms created by the second pulse leave the condensate later, but with a greater velocity than the atoms from the first pulse. When the two emitted waves overlap, they interfere and produce fringes (Fig. 3b). The phase of the fringes ϕ is given by the relative phase of the interfering matter waves, and varies with emission angle θ (Fig. 3c).

We observe the phase correlation of fringes along counter-propagating directions. In Fig. 3e, we present the occurrence distribution of the fringe phases in opposite directions, namely, ϕ_θ and $\phi_{\theta+\pi}$. The two phases correlate in such a way that they sum to a constant, $\phi_\theta+\phi_{\theta+\pi}=\phi_s$ (Fig. 3e,f) as a result of phase matching in a five-mixing process (Methods and ref. [17]).

To be more quantitative, we evaluate the phase correlation function $g_\pm(\varphi)$ for all angular spans φ (ref. [18]), defined as (Fig. 3g)

$$g_\pm(\varphi)=|\langle e^{i\phi_\theta \pm i\phi_{\theta+\varphi}}\rangle| \qquad (5)$$

here the angle brackets correspond to angular averaging over θ and ensemble averaging. The peak of g_+ at $\varphi=\pi$ confirms that fringe phases are only anticorrelated in opposite directions. The lone peak of g_- at $\varphi=0$ shows the phase coherence within a single jet.

Since jets with different energies are generated independently, the correlations of the fringes indicate the phase correlations of counter-propagating jets with the same momentum. Such phase correlation results from the coherent generation of atom pairs, which are phase locked to the modulation; the correlation is also expected for Unruh radiation[4], and resembles the phase coherence in the parametric down-conversion process in quantum optics[19].

Next we show the temporal coherence of the matter-wave radiation by reversing the time evolution. Similar experiments to reverse parametric amplification are realized based on photonic and atomic fields with two well-defined outgoing modes and low atom numbers[20–22], whereas the condensate in our system simultaneously couples to about 300 momentum modes and involves about 10^5 atoms.

Here we perform the experiment as follows: after modulating the scattering length, we jump the phase of the modulation by α (Fig. 4a). We monitor the evolution of the radiation patterns, from which we determine the total emitted atom number N (Fig. 4b). A clear suppression of atom number is shown for large phase jumps. We evaluate the suppression ratio $\eta(\alpha)=N_\alpha(\tau_c)/N_0(\tau_c)$ at time $\tau_c=5.76$ ms when the maximal reversal occurs (Fig. 4b). In particular, when $\alpha=\pi$, N reduces by as much as 51(3)% of that without the phase jump ($\alpha=0$). At $\alpha=\pi$, a reversal of 26(3)% (or 2,200 atoms) of the matter-wave excitations back to the condensate is observed. Our results are consistent with the theoretical simulation (Methods).

We evaluate entropy S and temperature T from the distribution of emitted atom number, which remains thermal before and after the phase jump (Fig. 4c). Here we compare them for the two cases with phase jump $\alpha=0$ and π. In the former case entropy S and temperature T continuously increase, while in the latter case both of them decrease first but eventually increase again. The reversal can be clearly seen from the strength of the emission pattern in the averaged images (Fig. 4d). The limited amount of reversal we can achieve is due to off-resonant coupling to the momentum modes close to $|\mathbf{k}|=k_f$ (Methods).

Remarkably the reversibility of the matter-wave emission suggests that the system undergoes a unitary evolution. The reversible entropy, together with the long-range coherence shown in Fig. 3, indicates that the matter-wave field remains a pure state after all, and the entropy extracted from local measurements potentially results from quantum entanglement between different momentum modes.

In conclusion, we have demonstrated a new type of quantum simulation to investigate quantum phenomena in a non-inertial frame. By simulating the Rindler frame transformation on the vacuum state, we observe the appearance of thermal radiation of matter waves that resembles Unruh radiation. Such matter-wave radiation, albeit thermal from local measurements, possesses long-range spatial and temporal coherence, which distinguishes it from classical thermal radiation.

Our method is readily applicable to generic quantum states, such as Fock states, superposition and entangled states, and can be extended to other frame transformations by spatially or temporally controlling the interaction modulation. As an example, the curved spacetime near a black hole could be simulated with an inhomogeneous acceleration that matches the gravitational pull near the black hole. Abundant intriguing topics exist at the interface of quantum mechanics and general relativity, such as Hawking radiation, black hole thermodynamics and the information paradox, which can be simulated in a bench-top experiment[23–28].

Online content

Any methods, additional references, Nature Research reporting summaries, source data, statements of code and data availability and associated accession codes are available at https://doi.org/10.1038/s41594-018-0123-8.

Received: 4 August 2018; Accepted: 15 April 2019;
Published online: 27 May 2019

References

1. Hawking, S. W. Black hole explosions? *Nature* **248**, 30–31 (1974).
2. Hawking, S. W. Particle creation by black holes. *Commun. Math. Phys.* **43**, 199–220 (1975).
3. Unruh, W. G. Notes on black-hole evaporation. *Phys. Rev. D* **14**, 870–892 (1976).
4. Wald, R. M. *Quantum Field Theory in Curved Spacetime and Black Hole Thermodynamics* (University of Chicago Press, 1994).
5. Bekenstein, J. D. Black holes and entropy. *Phys. Rev. D* **7**, 2333–2346 (1973).
6. Hawking, S. W. Black holes and thermodynamics. *Phys. Rev. D* **13**, 191–197 (1976).
7. Hayden, P. & Preskill, J. Black holes as mirrors: quantum information in random subsystems. *J. High Energy Phys.* **2007**, 120 (2007).
8. Giddings, S. B. Black holes, quantum information, and the foundations of physics. *Phys. Today* **66**, 30 (2013).
9. Clark, L. W., Gaj, A., Feng, L. & Chin, C. Collective emission of matter-wave jets from driven Bose-Einstein condensates. *Nature* **551**, 356–359 (2017).
10. Maldacena, J. The large n limit of superconformal field theories and supergravity. *Adv. Theor. Math. Phys.* **2**, 213–252 (2018).
11. Hawking, S. W. Breakdown of predictability in gravitational collapse. *Phys. Rev. D* **14**, 2460–2473 (1976).
12. Susskind, L. The paradox of quantum black holes. *Nat. Phys.* **2**, 665–677 (2006).
13. Almheiri, A., Marolf, D., Polchinski, J. & Sully, J. Black holes: complementarity or firewalls? *J. High Energy Phys.* **2013**, 62 (2013).
14. Su, D., Ho, C. T. M., Mann, R. B. & Ralph, T. C. Quantum circuit model for non-inertial objects: a uniformly accelerated mirror. *New J. Phys.* **19**, 063017 (2017).
15. Chin, C., Grimm, R., Julienne, P. & Tiesinga, E. Feshbach resonances in ultracold gases. *Rev. Mod. Phys.* **82**, 1225–1286 (2010).
16. Nguyen, J. H. V. et al. Parametric excitation of a Bose-Einstein condensate: from Faraday waves to granulation. *Phys. Rev. X* **9**, 011052 (2019).
17. Feng, L., Hu, J., Clark, L. W. & Chin, C. Correlations in high-harmonic generation of matter-wave jets revealed by pattern recognition. *Science* **363**, 521–524 (2019).
18. Langen, T., Geiger, R., Kuhnert, M., Rauer, B. & Schmiedmayer, J. Local emergence of thermal correlations in an isolated quantum many-body system. *Nat. Phys.* **9**, 640–643 (2013).
19. Howell, J. C., Bennink, R. S., Bentley, S. J. & Boyd, R. W. Realization of the Einstein-Podolsky-Rosen paradox using momentum- and position-entangled photons from spontaneous parametric down conversion. *Phys. Rev. Lett.* **92**, 210403 (2004).
20. Zheng, Y., Ren, H., Wan, W. & Chen, X. Time-reversed wave mixing in nonlinear optics. *Sci. Rep.* **3**, 3245 (2013).

21. Linnemann, D. et al. Quantum-enhanced sensing based on time reversal of nonlinear dynamics. *Phys. Rev. Lett.* **117**, 013001 (2016).
22. Linnemann, D. et al. Active SU(1,1) atom interferometry. *Quantum Sci. Technol.* **2**, 044009 (2017).
23. Garay, L. J., Anglin, J. R., Cirac, J. I. & Zoller, P. Sonic analog of gravitational black holes in Bose-Einstein condensates. *Phys. Rev. Lett.* **85**, 4643–4647 (2000).
24. Schützhold, R. & Unruh, W. G. Hawking radiation in an electromagnetic waveguide. *Phys. Rev. Lett.* **95**, 031301 (2005).
25. Horstmann, B., Reznik, B., Fagnocchi, S. & Cirac, J. I. Hawking radiation from an acoustic black hole on an ion ring. *Phys. Rev. Lett.* **104**, 250403 (2010).
26. Bekenstein, R., Schley, R., Mutzafi, M., Rotschild, C. & Segev, M. Optical simulations of gravitational effects in the Newton-Schrödinger system. *Nat. Phys.* **11**, 872–878 (2015).
27. Steinhauer, J. Observation of quantum Hawking radiation and its entanglement in an analogue black hole. *Nat. Phys.* **12**, 959–965 (2016).
28. Rodríguez-Laguna, J., Tarruell, L., Lewenstein, M. & Celi, A. Synthetic Unruh effect in cold atoms. *Phys. Rev. A* **95**, 013627 (2017).

Acknowledgements

We thank R. M. Wald, N. D. Gemelke and L. W. Clark for helpful discussions and reading the manuscript. We thank K. Levin's group for providing the numerical solver. We thank F. Fung for graphics preparation. L.F. acknowledges support from an MRSEC-funded graduate research fellowship. This work is supported by National Science Foundation (NSF) grant no. PHY-1511696, the Army Research Office Multidisciplinary Research Initiative under grant W911NF-14-1-0003 and the University of Chicago Materials Research Science and Engineering Center, which is funded by the NSF under grant no. DMR-1420709.

Author contributions

J.H. proposed this idea. J.H., L.F. and Z.Z. performed the experiments, built the theoretical model and analysed the data. C.C. supervised the work. All the authors contributed to discussing the results and writing the manuscript.

Competing interests

The authors declare no competing interests.

Additional information

Supplementary information is available for this paper at https://doi.org/10.1038/s41567-019-0537-1.

Reprints and permissions information is available at www.nature.com/reprints.

Correspondence and requests for materials should be addressed to J.H.

Journal peer review information: *Nature Physics* thanks Giovanni Modugno and the other anonymous reviewer(s) for their contribution to the peer review of this work.

Methods

Experimental methods. *Condensate preparation.* We start with Bose–Einstein condensates of 6×10^4 caesium atoms loaded into a disc-shaped trap with a radius of 7 µm (in Fig. 3) or 13 µm (in Figs. 2 and 4). The horizontal confinement is provided by a blue-detuned laser at 780 nm. The laser intensity profile is shaped by a digital micromirror device and projected to the atom plane through a high-resolution objective lens. The dipole trap provides a barrier height of $h\times300$ Hz beyond the radius of the trap. Atoms are tightly confined in the vertical direction to a root-mean-square radius of 0.5 µm with a harmonic trapping frequency of 220 Hz.

Scattering length modulation. After loading atoms into the dipole trap, we modulate the magnetic field near a Feshbach resonance, which causes the *s*-wave scattering length a of the atoms to oscillate as $a(\tau)=a_{\rm dc}+a_{\rm ac}\sin\omega\tau$. We maintain a small positive mean scattering length $a_{\rm dc}=4\,a_0$ throughout the experiment. In Fig. 2, the modulation frequency is $\omega=2\pi\times2.1$ kHz with amplitude $a_{\rm ac}=50\,a_0$. Different τ ranging from 0 to 7.68 ms are applied to monitor the evolution of the matter-wave emission. In Fig. 3, two pulses with $\omega=2\pi\times3$ and $2\pi\times5.63$ kHz, $a_{\rm ac}=56\,a_0$ and $72\,a_0$ and a relative phase δ are applied to generate two sets of jets with different propagation speeds. In Fig. 4, two pulses with the same $\omega=2\pi\times2.1$ kHz and amplitude $a_{\rm ac}=50\,a_0$ are applied. A tunable phase jump between the two pulses serves to optimize the reversal of the matter-wave radiation.

Detection technique. For the experiment in Fig. 4, we perform time-of-flight measurements in a weak radial harmonic trap to focus emitted atoms with the same momentum, and thus determine the atom number with a higher signal-to-noise ratio[29]. At the end of the modulation, we wait for 0.5 ms and then turn on the harmonic confinement from a dipole trap while maintaining the disc-shaped trap. Atoms with the same momentum are focused to the same location after a quarter harmonic trap period (the trap period is 80 ms), when the imaging is performed to extract the atom number.

To measure the thermal distribution of atoms in a jet and the phase from the jet interference pattern, we perform in situ imaging in free space without the harmonic trap to preserve the jet structure. For the thermal distribution measurement, we image the atoms 30 ms after the beginning of the magnetic field modulation. We evaluate the atom number in every 2° slice of typically 15 images taken under the same conditions, from which we build the histogram of the atomic distribution. To extract the phases from jet interferences, atoms are imaged 13.5 ms after the beginning of the magnetic field modulation. A 15° bin is chosen and the radial atomic density interference curve is obtained by integrating and fitting the atomic density over the angle within each slide. A collection of 200 images is used for the data presented in Fig. 3.

Equivalence of time evolution and Rindler frame transformation. The time evolution under the Hamiltonian $\mathcal{H}={\rm i}\hbar\sum_k g_k(a_k^\dagger a_{-k}^\dagger-a_ka_{-k})$ is governed by the equation of state, which is given in the Heisenberg picture as

$$\dot{a}_k=\frac{\rm i}{\hbar}[H,a_k]=g_ka_{-k}^\dagger \tag{6}$$

$$\dot{a}_{-k}=\frac{\rm i}{\hbar}[H,a_{-k}]=g_ka_k^\dagger \tag{7}$$

The solution is

$$\begin{bmatrix}a_k(\tau)\\a_{-k}^\dagger(\tau)\end{bmatrix}=\begin{bmatrix}\cosh(g_k\tau)&\sinh(g_k\tau)\\\sinh(g_k\tau)&\cosh(g_k\tau)\end{bmatrix}\begin{bmatrix}a_k(0)\\a_{-k}^\dagger(0)\end{bmatrix} \tag{8}$$

On the other hand, let us consider a different problem of describing a scalar quantum field in an accelerating reference frame. The frame transformation, called the Rindler transformation, is given by[14]

$$\begin{bmatrix}\hat{b}_k^{\rm R}\\\hat{b}_k^{\dagger{\rm L}}\end{bmatrix}=\begin{bmatrix}\cosh(r_k)&\sinh(r_k)\\\sinh(r_k)&\cosh(r_k)\end{bmatrix}\begin{bmatrix}\hat{c}_k\\\hat{d}_k^\dagger\end{bmatrix} \tag{9}$$

where $\hat{b}_k^{\rm R}$ and $\hat{b}_k^{\rm L}$ are the annihilation operators of 'Rindler modes' with energy E_k in the accelerating frame, L and R refer to the two Rindler wedges and $\hat{c}_k$ and $\hat{d}_k$ are the annihilation operators of 'Unruh modes' in the inertial frame. The parameter r_k is related to the acceleration as $\tanh r_k={\rm e}^{-\pi E_kc/\hbar A}$.

Remarkably, equations (8) and (9) share the same mathematical expression. We can thus simulate a quantum system in an accelerating frame by engineering the evolution operator shown in equation (8) to match the Rindler transformation in equation (9). Given the same transformation for all the relevant operators, what a generic wave function would look like in an accelerating frame can be simulated by the engineered time evolution of the system, shown in equation (1). Here g_k is linked to A by

$$g_k=\frac{1}{2\tau}\ln\coth\left(\frac{\pi E_kc}{2\hbar A}\right) \tag{10}$$

Evolution and observables of condensates with modulated interactions. We start with the second-quantization form of the Hamiltonian

$$\begin{aligned}H=&\int{\rm d}^3\mathbf{r}\;\Psi^\dagger(\mathbf{r},\tau)\frac{p^2}{2m}\Psi(\mathbf{r},\tau)\\&+\frac{\tilde{g}(\tau)}{2}\int{\rm d}^3\mathbf{r}\;\Psi^\dagger(\mathbf{r},\tau)\Psi^\dagger(\mathbf{r},\tau)\Psi(\mathbf{r},\tau)\Psi(\mathbf{r},\tau)\end{aligned} \tag{11}$$

where $\tilde{g}(\tau)=4\pi\hbar^2a(\tau)/m$ is the coupling constant and is proportional to the scattering length. In our experiment, the scattering length is modulated as $a(\tau)=a_{\rm dc}+a_{\rm ac}\sin\omega\tau$. By applying the Fourier transformation of the field operator

$$\Psi(\mathbf{r},\tau)=\frac{1}{\sqrt{V}}\sum_k{\rm e}^{{\rm i}\mathbf{k}\cdot\mathbf{r}}a_{\mathbf{k}} \tag{12}$$

where V is the volume of the condensate, we obtain the Hamiltonian in the momentum space as

$$H=\sum_{\mathbf{k}}\epsilon_ka_{\mathbf{k}}^\dagger a_{\mathbf{k}}+\frac{\tilde{g}(\tau)}{2V}\sum_{\mathbf{k}_1,\mathbf{k}_2,\Delta\mathbf{k}}a_{\mathbf{k}_1+\Delta\mathbf{k}}^\dagger a_{\mathbf{k}_2-\Delta\mathbf{k}}^\dagger a_{\mathbf{k}_1}a_{\mathbf{k}_2} \tag{13}$$

In the interaction picture, we eliminate the kinetic energy term $H_0=\sum_{\mathbf{k}}\epsilon_ka_{\mathbf{k}}^\dagger a_{\mathbf{k}}$ by transferring the operators for atoms into a rotating frame with $a_{\mathbf{k}}\to a_{\mathbf{k}}{\rm e}^{{\rm i}\epsilon_{\mathbf{k}}\tau/\hbar}$ and ignore the fast-varying terms. We further simplify the Hamiltonian under the Bogoliubov approximation $a_0\approx\sqrt{N_0}$ ($N_0\gg1$), and apply energy–momentum conservation $\hbar\omega=\hbar^2k_{\rm f}^2/m$. The resulting Hamiltonian reduces to

$$H={\rm i}\hbar g\sum_{|\mathbf{k}|=k_{\rm f}}(a_k^\dagger a_{-k}^\dagger-a_ka_{-k}) \tag{14}$$

where $g=\pi\hbar N_0a_{\rm ac}/mV$ is the coupling constant.

According to equation (8), we can write the equation of motion as

$$\begin{bmatrix}a_k(\tau)\\a_{-k}^\dagger(\tau)\end{bmatrix}={\rm e}^{g\tau\sigma_x}\begin{bmatrix}a_k(0)\\a_{-k}^\dagger(0)\end{bmatrix} \tag{15}$$

where σ_x is the *x*-component of the Pauli matrices. The evolution matches the Rindler transformation equation (9) with the simulated acceleration

$$A=\frac{\pi\omega c}{2\ln\coth(g\tau)} \tag{16}$$

To simulate the Unruh radiation, we initialize the condensate in the ground state with negligible excitations $N_k\approx0$ for $|k|>0$. After the modulation begins, the mean population in a mode increases as $\bar{n}=\langle a_k^\dagger(\tau)a_k(\tau)\rangle=\sinh^2(g\tau)$. Thus we can also relate A to the mean population as

$$A=\frac{2\pi cE}{\hbar\ln(1+1/\bar{n})}\xrightarrow[\bar{n}\gg1]{}\frac{2\pi cE}{\hbar}\bar{n} \tag{17}$$

where $E=\hbar\omega/2$ is the kinetic energy of each excited atom.

Next let us consider the evolution of the wave function. Since the modulation generates pairs of counter-propagating atoms with momenta k and $-k$, we can rewrite the Hamiltonian as $H=\sum_{k>0}h_k$, where $h_k={\rm i}\hbar g(a_k^\dagger a_{-k}^\dagger-a_ka_{-k})$. In the following we only consider the evolution of one h_k. To simplify the notation without loss of generality, we use h to replace h_k. The solution of the wave function is[30]

$$|\psi(\tau)\rangle={\rm e}^{-{\rm i}h\tau/\hbar}\,|0\rangle=\frac{1}{\cosh(g\tau)}\sum_{n=0}^{\infty}\tanh^n(g\tau)\,|n,n\rangle \tag{18}$$

where $|0\rangle$ is the vacuum state at $\tau=0$, and the ket $|n,n\rangle$ indicates that there are n and n particles in the modes with momentum k and $-k$, respectively.

The above wave function is the same as a Minkovski vacuum state expressed in the basis of the Rindler coordinate[4]. The reduced density matrix of one single mode such as k can be determined by tracing out the other mode $-k$, which yields

$$\hat{\rho}(\tau)={\rm Tr}_{-k}\,|\psi(\tau)\rangle\,\langle\psi(\tau)|=\sum_{n=0}^{\infty}p_n\,|n\rangle_k\langle n|_k \tag{19}$$

where $p_n=\tanh^{2n}(g\tau)/\cosh^2(g\tau)$ is the probability of n particles in the mode. By comparing with a thermal distribution of bosons in a quantum state

$$p_{\mathrm{th}}(n) = \mathrm{e}^{-\frac{n\hbar\omega}{2k_{\mathrm{B}}T}}(1 - \mathrm{e}^{-\frac{\hbar\omega}{2k_{\mathrm{B}}T}}) \tag{20}$$

we see that $\hat{\rho}(\tau)$ describes a thermal state with temperature given by

$$T = \frac{E}{2k_{\mathrm{B}}\ln\coth(g\tau)} \tag{21}$$

$$= \frac{E}{k_{\mathrm{B}}\ln(1+1/\bar{n})} \xrightarrow[\bar{n}\gg1]{} \frac{E}{k_{\mathrm{B}}}\bar{n} \tag{22}$$

and the mean population

$$\bar{n} = \sum_{n=0}^{\infty} np_n = \frac{1}{\mathrm{e}^{E/k_{\mathrm{B}}T} - 1} \tag{23}$$

follows the Bose–Einstein distribution.

We also evaluate the entropy of atoms in a mode. The von Neumann entropy $S = -k_{\mathrm{B}}\mathrm{Tr}(\hat{\rho}(\tau)\ln\hat{\rho}(\tau))$ can be directly calculated as

$$S = 2k_{\mathrm{B}}[\ln\cosh(g\tau) + \sinh^2(g\tau)\ln\coth(g\tau)] \tag{24}$$

$$= k_{\mathrm{B}}\left[\ln(\bar{n}+1) + \bar{n}\ln\frac{\bar{n}+1}{\bar{n}}\right] \xrightarrow[\bar{n}\gg1]{} k_{\mathrm{B}}\ln(e\bar{n}) \tag{25}$$

where $e = 2.718...$ is Euler's number.

Using equation (16), we can relate the temperature to the simulated acceleration as

$$T = \frac{\hbar A}{2\pi c k_{\mathrm{B}}} \tag{26}$$

which is identical to the Unruh prediction shown in equation (2).

Equations (22) and (25), plotted in Fig. 2b, are in excellent agreement with the experimental measurement. In the next section, we will show that they are also identical to the thermodynamic expectation. The agreements support the description of the matter-wave radiation as a thermal field with Unruh temperature T_{U}.

Finally, together with equation (25), we obtain the thermodynamic relation between S and T as

$$S = -k_{\mathrm{B}}\left[\ln(\mathrm{e}^{E/k_{\mathrm{B}}T} - 1) - \frac{E/k_{\mathrm{B}}T}{(1 - \mathrm{e}^{-E/k_{\mathrm{B}}T})}\right] \xrightarrow[\bar{n}\gg1]{} k_{\mathrm{B}}\ln\left(\frac{ek_{\mathrm{B}}T}{E}\right) \tag{27}$$

Determination of mode width and effective temperature. In this section, we first determine the mode width experimentally. In ref. [9], measurement of the second-order correlation function $g^{(2)}(\theta)$ of Bose fireworks was reported. We have $g^{(2)}(0) = 2$, indicating that in one mode there is a relation of $\Delta n_{\mathrm{M}}^2 = [g^{(2)}(0) - 1]\langle n_{\mathrm{M}}\rangle^2$ where $\langle n_{\mathrm{M}}\rangle$ and Δn_{M}^2 are the mean and variance of the atom number.

Experimentally we slice our emission patterns into 180 slices and count the atom number in each slice. On the basis of the histogram of atom counting from the measurements, we build $P(n)$ and calculate $\langle n\rangle = \int nP(n)\mathrm{d}n$ and $\Delta n^2 = \langle n^2\rangle - \langle n\rangle^2 - \Delta n_{\mathrm{noise}}^2$. Here $\Delta n_{\mathrm{noise}}^2$ is the variance contributed from the detection noise which is statistically independent of the signal from atom counting. From this, we find a linear dependence between the mean atom number squared and the variance from the experiment as (Supplementary Fig. 1)

$$\langle n\rangle^2 = \xi\ \Delta n^2 \tag{28}$$

Here $\xi = \Delta\theta_S/\Delta\theta_J = 1.49(7)$ is determined from the fit and is insensitive to the atom number calibration. This ratio also characterizes the ratio between the mode width $\Delta\theta_J$ and the width of the slice $\Delta\theta_S = 2°$. Therefore, we obtain $\Delta\theta_J = 1.30°$. Alternatively, we can calculate $\Delta\theta_J$ independently. Using the formula $\Delta\theta_J = 1.62/(Rk_{\mathrm{f}})$ in ref. [9], which arises from the half width at half maximum of the peak at $\phi = 0$ in the $g^{(2)}$ function, we obtain a consistent result of $\Delta\theta_J = 1.33°$.

To test and verify that the emitted atom number in each mode follows a thermal distribution, we derive a more general formula for the probability distribution $p(n, \xi)$ in a slice with any width $\Delta\theta_S = \xi\Delta\theta_J$. Because the mean population per mode $\langle n_{\mathrm{M}}\rangle$ is always larger than 1 in our measurements, we treat the distribution $p(n, \xi)$ as a continuous function where the summation $\sum_{n=0}^{\infty} p(n, \xi) = 1$ is replaced by an integral $\int_0^{\infty}\mathrm{d}n\ p(n, \xi) = 1$.

Here we would like to list a few properties of the function $p(n, \xi)$. First, $p(n, \xi)$ must be equal to 0 when n is a negative number. Second, if the angular slice only contains one momentum mode (that is, $\xi = 1$), $p(n, 1)$ should be a thermal distribution, where $p(n, 1) = \beta\,\mathrm{e}^{-\beta n}$ with $\beta = E/k_{\mathrm{B}}T$. Third, the $p(n, \xi)$ have to satisfy the addition rule that combining two slices of ξ_1 and ξ_2 will create a new slice of $\xi_1 + \xi_2$. We can write the third requirement more explicitly as a mathematical equation

$$p(n, \xi_1 + \xi_2) = \int_{-\infty}^{\infty} p(n', \xi_1)p(n - n', \xi_2)\mathrm{d}n' \tag{29}$$

From all the above conditions, we solve the probability distribution $p(n, \xi)$ analytically as

$$p(n, \xi) = \begin{cases} \beta^{\xi}n^{\xi-1}\mathrm{e}^{-\beta n}/\Gamma(\xi) & n \geq 0 \\ 0 & n < 0 \end{cases} \tag{30}$$

where $\Gamma(\xi)$ is the gamma function.

In addition to the signals from the atoms, the detection noise contributes to the measured probability distribution of the atom number. Experimentally we characterize this noise distribution $G(n, \xi)$ by inspecting the images without any radiation. Once we obtain $G(n, \xi)$, we convolve it with $p(n, \xi)$ to give a full distribution function

$$P(n, \xi) = \int_{-\infty}^{\infty}\mathrm{d}n' p(n', \xi)G(n - n', \xi) \tag{31}$$

Then we use this function to fit our data extracting T under the condition $\xi = 1.5$ (Supplementary Fig. 1b).

Characterization of entropy from population distribution. We define the entropy in one slice with width $\xi\,\Delta\theta_J$ as $S(\xi)$. First we use the probability distribution $p(n, \xi)$ derived in the previous section to evaluate $S(\xi)$, which gives

$$\begin{aligned} S(\xi)/k_{\mathrm{B}} &= -\int_{-\infty}^{\infty}\mathrm{d}n\ p(n, \xi)\ln p(n, \xi) \\ &= -\ln\beta + \xi + \ln\Gamma(\xi) - (\xi - 1)\Gamma'(\xi)/\Gamma(\xi) \end{aligned} \tag{32}$$

In our data analysis, we divide the radiation pattern into 180 slices and determine the probability distribution $P(n)$. Thus, the entropy directly measured by the experiment is

$$S(1.5) = -k_{\mathrm{B}}\sum_n P(n)\ln P(n) \tag{33}$$

We show that the entropy in a single mode $S(1)$ is given by

$$S(1) = S(1.5) - S_0 = -k_{\mathrm{B}}\sum_n P(n)\ln P(n) - S_0 \tag{34}$$

on the basis of equation (32), where $S_0 = k_{\mathrm{B}}[\xi - 1 + \ln\Gamma(\xi) - (\xi - 1)\Gamma'(\xi)/\Gamma(\xi)]|_{\xi=1.5} = 0.37k_{\mathrm{B}}$.

For the theoretical curve with noise plotted in Fig. 2b (blue solid line), we characterize the detection noise per mode $G(n, 1)$ and then evaluate the theoretical distribution by convolving $G(n, 1)$ with $p(n, 1)$ as

$$\tilde{P}(n, 1) = \int_{-\infty}^{\infty}\mathrm{d}n'\ p(n', 1)G(n - n', 1) \tag{35}$$

and we calculate the entropy as

$$S = -k_{\mathrm{B}}\int\mathrm{d}n\ \tilde{P}(n, 1)\ln\tilde{P}(n, 1) \tag{36}$$

which matches our experimental data (see the blue solid line in Fig. 2b). The purple line shows the calculation in the absence of detection noise.

In summary, the agreement between experiment and theory shows that the matter-wave radiation from the condensate matches the thermodynamic expectation from a Bose gas at zero chemical potential $\mu = 0$ and $T = T_{\mathrm{U}}$.

Phase correlations of atomic radiation field. Here we calculate the phase correlations between interference fringes, which directly relate to those between emitted jets. We consider two sets of independent jets generated by two pulses of scattering length modulation with a certain phase. In the interaction picture, the wave function can be written as $|\psi\rangle_{\mathrm{I}} = |\psi^{(1)}\rangle_{\mathrm{I}} \otimes |\psi^{(2)}\rangle_{\mathrm{I}}$. Each $|\psi^{(j)}\rangle_{\mathrm{I}}$ follows

$$|\psi^{(j)}\rangle_{\mathrm{I}} = \frac{1}{\cosh(\gamma_j)}\sum_{n=0}^{\infty}[\mathrm{e}^{\mathrm{i}(\phi_{M_j} - \pi/2)}\tanh(\gamma_j)]^n\ |n, n\rangle_{k_j, -k_j} \tag{37}$$

under the Hamiltonian

$$H_{\mathrm{I}}^{(i)} = g_j\ \mathrm{e}^{\mathrm{i}\phi_{M_j}}a_{k_j}^{\dagger}a_{-k_j}^{\dagger} + g_j\ \mathrm{e}^{-\mathrm{i}\phi_{M_j}}a_{k_j}a_{-k_j} \tag{38}$$

where ϕ_{M_j} is given by the phase of the external driving field, $\gamma_j = g_j\tau_j$ and τ_j is the modulation duration of the pulse.

To take the dynamical phase into account, we convert the wave function back to Schrödinger's picture, and the wave function is written as

$$|\psi\rangle_S = |\psi^{(1)}\rangle_S \otimes |\psi^{(2)}\rangle_S \tag{39}$$

where $|\psi^{(j)}\rangle_S$ is given by

$$\begin{aligned} |\psi^{(j)}\rangle_S &= \mathrm{e}^{-\mathrm{i}H_0^{(j)}t/\hbar}\ |\psi^{(j)}\rangle_\mathrm{I} \\ &= \frac{1}{\cosh(\gamma_j)} \sum_{n=0}^{\infty} [\mathrm{e}^{\mathrm{i}(\phi_{M_j} - \omega_j t - \pi/2)} \tanh(\gamma_j)]^n\ |n, n\rangle_{k_j, -k_j} \end{aligned} \tag{40}$$

Here $H_0^{(i)} = \hbar\omega_i(a^\dagger_{\mathbf{k}_j} a_{\mathbf{k}_j} + a^\dagger_{-\mathbf{k}_j} a_{-\mathbf{k}_j})/2$ is the energy term that was previously eliminated in the interaction picture.

The interference operators between the two sets of jets are $\hat{I}_\mathrm{f} = a_{\mathbf{k}_1} a^\dagger_{\mathbf{k}_2}$ and $\hat{I}_\mathrm{b} = a_{-\mathbf{k}_1} a^\dagger_{-\mathbf{k}_2}$, which correspond to the forward and backward directions. We introduce four more interference operators as $\hat{I}_{j+} = a_{\mathbf{k}_j} a_{-\mathbf{k}_j}$ and $\hat{I}_{j-} = a_{\mathbf{k}_j} a^\dagger_{-\mathbf{k}_j}$ with $j = 1$ or 2. The mean value for the interference operator $\hat{I}_{i\pm}$ is evaluated as

$$\begin{aligned} \left\langle \hat{I}_{j+} \right\rangle &= \langle \psi^{(j)}|_S\ (a_{\mathbf{k}_j} a_{-\mathbf{k}_j})\ |\psi^{(j)}\rangle_S \\ &= \sqrt{\left\langle n_j \right\rangle (\left\langle n_j \right\rangle + 1)}\, e^{i(\phi_{M_j} - \omega_j t - \pi/2)} \end{aligned} \tag{41}$$

$$\begin{aligned} \left\langle \hat{I}_{j-} \right\rangle &= \langle \psi^{(j)}|_S\ (a_{\mathbf{k}_j} a^\dagger_{-\mathbf{k}_j})\ |\psi^{(j)}\rangle_S \\ &= 0 \end{aligned} \tag{42}$$

where $\langle n_j \rangle$ is the mean atom number in each set of jets.

Phase correlation between interference fringes can be directly decomposed into the interference operators in each set of jets. The phase correlation $g_+(\theta = \pi)$ is proportional to the correlation between $\hat{I}_\mathrm{f}$ and $\hat{I}_\mathrm{b}$; together with equation (41) we obtain

$$\begin{aligned} &\langle \mathrm{e}^{\mathrm{i}(\phi_\theta + \phi_{\theta+\pi})} \rangle \propto \langle \hat{I}_\mathrm{f} \hat{I}_\mathrm{b} \rangle \\ &= \langle \psi^{(1)}|_S \otimes \langle \psi^{(2)}|_S\ (a_{\mathbf{k}_1} a^\dagger_{\mathbf{k}_2} a_{-\mathbf{k}_1} a^\dagger_{-\mathbf{k}_2})\ |\psi^{(1)}\rangle_S \otimes |\psi^{(2)}\rangle_S \\ &= \langle \psi^{(1)}|_S\ (a_{\mathbf{k}_1} a_{-\mathbf{k}_1})\ |\psi^{(1)}\rangle_S \langle \psi|^{(2)}_S\ (a^\dagger_{\mathbf{k}_2} a^\dagger_{-\mathbf{k}_2})\ |\psi\rangle^{(2)}_S \\ &= \langle \hat{I}_{1+} \rangle \langle \hat{I}^\dagger_{2+} \rangle \\ &= \sqrt{\langle n_1 \rangle (\langle n_1 \rangle + 1)}\, \sqrt{\langle n_2 \rangle (\langle n_2 \rangle + 1)}\, \mathrm{e}^{\mathrm{i}[(\phi_{M_1} - \phi_{M_2}) - (\omega_1 - \omega_2)t]} \end{aligned} \tag{43}$$

Therefore, the sum of the phases of the forward and backward interference fringes depends only on the phase of the driving and the dynamical phase. Thus we have the phase constant $\phi_\mathrm{s} = \phi_\theta + \phi_{\theta+\pi} = (\phi_{M_1} - \phi_{M_2}) - (\omega_1 - \omega_2)t$ and $g_+(\pi) = 1$.

Meanwhile, the phase correlation $g\_(\theta = \pi)$ is proportional to the mean value of $\hat{I}_\mathrm{f} \hat{I}^\dagger_\mathrm{b}$; together with equation (42) we have

$$\begin{aligned} &\langle \mathrm{e}^{\mathrm{i}\phi_\theta - \phi_{\theta+\pi}} \rangle \propto \langle \hat{I}_\mathrm{f} \hat{I}^\dagger_\mathrm{b} \rangle \\ &= \langle \psi^{(1)}|_S \otimes \langle \psi^{(2)}|_S\ (a_{\mathbf{k}_1} a^\dagger_{\mathbf{k}_2} a^\dagger_{-\mathbf{k}_1} a_{-\mathbf{k}_2})\ |\psi^{(1)}\rangle_S \otimes |\psi^{(2)}\rangle_S \\ &= \langle \psi^{(1)}|_S\ (a_{\mathbf{k}_1} a^\dagger_{-\mathbf{k}_1})\ |\psi^{(1)}\rangle_S \langle \psi^{(2)}|_S\ (a^\dagger_{\mathbf{k}_2} a_{-\mathbf{k}_2})\ |\psi^{(2)}\rangle_S \\ &= \langle \hat{I}_{1-} \rangle \langle \hat{I}^\dagger_{2-} \rangle \\ &= 0 \end{aligned} \tag{44}$$

therefore, we have $g\_(\pi) = 0$, indicating that phases in each pair of jets are totally random although their sum is fixed. The results from equations (43) and (44) are consistent with our measurement shown in Fig. 3g.

We also derive analytic formulas for the phase correlation functions $g_+(\theta)$ and $g\_(\theta)$ between two arbitrary angular directions, in addition to that between the counter-propagating directions in equations (43) and (44), as follows:

$$g_+(\theta) = \left| \frac{\langle a_{\mathbf{k}_1} a^\dagger_{\mathbf{k}_2} a_{\mathbf{k}'_1} a^\dagger_{\mathbf{k}'_2} \rangle}{\langle a^\dagger_{\mathbf{k}_1} a_{\mathbf{k}_1} \rangle \langle a^\dagger_{\mathbf{k}_2} a_{\mathbf{k}_2} \rangle} \right| = \left| \frac{\langle a_{\mathbf{k}_1} a_{\mathbf{k}'_1} \rangle \langle a^\dagger_{\mathbf{k}_2} a^\dagger_{\mathbf{k}'_2} \rangle}{\langle a^\dagger_{\mathbf{k}_1} a_{\mathbf{k}_1} \rangle \langle a^\dagger_{\mathbf{k}_2} a_{\mathbf{k}_2} \rangle} \right| \tag{45}$$

$$g\_(\theta) = \left| \frac{\langle a_{\mathbf{k}_1} a^\dagger_{\mathbf{k}_2} a^\dagger_{\mathbf{k}'_1} a_{\mathbf{k}'_2} \rangle}{\langle a^\dagger_{\mathbf{k}_1} a_{\mathbf{k}_1} \rangle \langle a^\dagger_{\mathbf{k}_2} a_{\mathbf{k}_2} \rangle} \right| = \left| \frac{\langle a_{\mathbf{k}_1} a^\dagger_{\mathbf{k}'_1} \rangle \langle a^\dagger_{\mathbf{k}_2} a_{\mathbf{k}'_2} \rangle}{\langle a^\dagger_{\mathbf{k}_1} a_{\mathbf{k}_1} \rangle \langle a^\dagger_{\mathbf{k}_2} a_{\mathbf{k}_2} \rangle} \right| \tag{46}$$

Here $\mathbf{k}_1$ and $\mathbf{k}_2$ are the momenta of jets created from different modulations and propagate along the same direction, while $\mathbf{k}'_1$ and $\mathbf{k}'_2$ represent another pair of such co-propagating jets along the direction with a relative angle of θ to that of $\mathbf{k}_1$ and $\mathbf{k}_2$. In the spirit of ref. [9] and taking the finite size of the condensate into consideration, we obtain

$$\left\langle a_{\mathbf{k}_j} a_{\mathbf{k}'_j} \right\rangle = \mathrm{e}^{\mathrm{i}(\phi_{M_j} - \omega_j\tau - \pi/2)} \frac{\tilde{\rho}(\mathbf{k}_j + \mathbf{k}'_j)}{2\pi} \cosh(\gamma_j)\sinh(\gamma_j) \tag{47}$$

$$\left\langle a^\dagger_{\mathbf{k}_j} a_{\mathbf{k}'_j} \right\rangle = \frac{\tilde{\rho}(\mathbf{k}_j - \mathbf{k}'_j)}{2\pi} \sinh^2(\gamma_j) \tag{48}$$

where $\tilde{\rho}(\mathbf{k})$ is defined as the Fourier transformation of a uniform disc-shaped density $\rho(\mathbf{r})$:

$$\rho(\mathbf{r}) = \frac{1}{2\pi} \int \mathrm{d}^2\mathbf{k}\ \mathrm{e}^{\mathrm{i}\mathbf{k}\cdot\mathbf{r}} \tilde{\rho}(\mathbf{k}) \tag{49}$$

and $\rho(\mathbf{r})$ is the density distribution function of the condensate:

$$\rho(\mathbf{r}) = \begin{bmatrix} 1 & |\mathbf{r}| \le R \\ 0 & |\mathbf{r}| > R \end{bmatrix} \tag{50}$$

with R the condensate radius. Therefore, the analytic formulas for $g_\pm(\theta)$ when $\gamma_j \gg 1$ and $|\mathbf{k}_i| R \gg 1$ are

$$\begin{aligned} g_+(\theta) &= \left| \frac{\tilde{\rho}(\mathbf{k}_1 + \mathbf{k}'_1) \tilde{\rho}^*(\mathbf{k}_2 + \mathbf{k}'_2)}{4\pi^2} \right| \\ &= \left| \frac{4 J_1(|\mathbf{k}_1| R(\theta - \pi)) J_1(|\mathbf{k}_2| R(\theta - \pi))}{|\mathbf{k}_1||\mathbf{k}_2| R^2 (\theta - \pi)^2} \right| \end{aligned} \tag{51}$$

and

$$\begin{aligned} g\_(\theta) &= \left| \frac{4\tilde{\rho}(\mathbf{k}_1 - \mathbf{k}'_1) \tilde{\rho}^*(\mathbf{k}_2 - \mathbf{k}'_2)}{\tilde{R}^4} \right| \\ &= \left| \frac{J_1(|\mathbf{k}_1| R\theta) J_1(|\mathbf{k}_2| R\theta)}{|\mathbf{k}_1||\mathbf{k}_2| 4\pi^2 \theta^2} \right| \end{aligned} \tag{52}$$

where $J_1(x)$ is the first-order Bessel function of the first kind.

To experimentally extract the interference fringe phase ϕ_θ for a particular emission direction θ, we average over an angular span from $\theta - 0.12$ to $\theta + 0.12$ to obtain the radial density distribution $\rho(r,\theta)$ to achieve the best signal-to-noise ratio (Fig. 3d). We then perform Fourier transformation on the radial density to obtain the complex density amplitude of the interference fringes in momentum space $\rho(k, \theta)$. The phase ϕ_θ at k_f is then evaluated from this complex amplitude. Although our jet width is small, that is 2° for $\omega/2\pi = 3$ kHz and 1.5° for $\omega/2\pi = 5.63$ kHz, this average results in a significantly broadened phase correlation, shown in Fig. 3g. To experimentally extract the phase constant ϕ_s, we fit the histogram of $\phi_\theta + \phi_{\theta+\pi}$ to obtain the peak position. We also calculate the expected phase shift on the basis of our experimental sequence with a time of 18.5 ms from the start of the modulation to the start of imaging. The first sinusoidal modulation pulse lasts for 7 periods while the second lasts for 16 periods. Meanwhile we take into account the time delay of the modulation pulse of 0.041 ms due to the system response. Therefore, the phase constant estimated from our experimental sequence is 0.9(2), where the uncertainty arises from the duration of our 20 μs imaging pulse.

Numerical results on reversal of atomic radiation field. In this section, we use numerical simulation based on a dynamical Gross–Pitaevskii equation to investigate the partial reversal on radiating matter-wave fields. We find that the results of this imperfect reversal mostly originate from the off-resonant coupling to finite momentum modes close to $|\mathbf{k}| = k_\mathrm{f}$.

Here we start with the Gross–Pitaevskii equation

$$\begin{aligned} \mathrm{i}\hbar \frac{\partial \psi}{\partial t} = &\left[-\frac{\hbar^2}{2m} \nabla^2 + V(\mathbf{r}) + U_\mathrm{dc} |\psi|^2 - \mu \right] \psi \\ &+ U_\mathrm{ac} f(t) |\psi|^2\, \psi \end{aligned} \tag{53}$$

where ψ is the wave function and $\mu = 2\pi\hbar \times 19$ Hz is the static chemical potential of the condensate, $V(r)$ is the disc-shaped trapping potential as a function of radius r, with $V(r) = 2\pi\hbar \times 300$ Hz for $13.6\ \mu\mathrm{m} \ge r \ge 13\ \mu\mathrm{m}$ and $V(r) = 0$ for the rest, and $U_\mathrm{dc} = 4\pi\hbar^2 a_\mathrm{dc}/m$ and $U_\mathrm{ac} = 4\pi\hbar^2 a_\mathrm{ac}/m$ are the d.c. and a.c. interaction strengths, with $a_\mathrm{dc} = 4\, a_0$ and $a_\mathrm{ac} = 50\, a_0$. In addition, we have $f(\tau) = \sin(\omega\tau)$ when $\tau \le 4.76$ ms and $f(\tau) = \sin(\omega\tau + \alpha)$ for $\tau > 4.76$ ms. These parameters are chosen according to our experimental conditions.

The results from simulation using a CUDA-based solver[31] show excellent agreement with the experiment. First of all, the total emitted atom number is suppressed after a phase jump close to π (see Supplementary Fig. 2a). The suppression sensitively depends on the phase of the second pulse. Similarly to the analysis of our experimental data, we then look at the suppression ratio as a function of α at $\tau_c = 5.62\,\mathrm{ms}$, when the optimal suppression appears (Supplementary Fig. 2c). The suppression ratio varies as a function of α in the same way as in our experiment and the best suppression that can be achieved is $\eta = 0.57$, comparable to the experimental result.

The reason for this partial suppression is the off-resonant coupling to modes with momentum slightly different from the resonant value $|\mathbf{k}| = k_f$. We examine carefully the emitted atoms in different momentum modes (Supplementary Fig. 2b), and find that not all the excited atoms have the resonant momentum. Instead, atoms spread across a range of momentum modes due to the uncertainty principle. Since the condensate has a finite radius of 13 μm, even if we apply a long driving pulse, the atoms effectively see modulation for a limited time before jets escape from the condensate. The finite modulation duration gives a finite bandwidth in the frequency domain centred around the modulation frequency. Thus atom pairs can be off-resonantly excited with energy that deviates from the energy quantum of the modulation, which evolves differently from the resonantly excited atom pairs, and the populations in these off-resonant modes are optimally reversed at different phase jumps. For any one particular momentum pair, the population reversal can reach 70% according to our calculation, while the total excited population can be reversed by no more than 50%, consistent with our measurement.

In addition to this off-resonant coupling, we anticipate that the reversal can be limited by other effects such as the fast counter-rotating terms and the motion of the emitted atoms as well. The counter-rotating terms lead to the quick population oscillations seen in Supplementary Fig. 2a; they also accumulate phase and eventually limit the reversal. Furthermore, when atoms move out of the condensate, they cannot be transferred back to the condensate again. These effects are included in the simulation but their contributions to the limited reversal are hard to separate in our numerical model.

Data availability

The data that support the plots within this paper and other findings of this study are available from the corresponding author on reasonable request.

References

29. Feng, L., Clark, L. W., Gaj, A. & Chin, C. Coherent inflationary dynamics for Bose-Einstein condensates crossing a quantum critical point. *Nat. Phys.* **14**, 269–272 (2018).
30. Wang, X.-B., Hiroshima, T., Tomita, A. & Hayashi, M. Quantum information with gaussian states. *Phys. Rep.* **448**, 1–111 (2007).
31. Clark, L. W. et al. Observation of density-dependent gauge fields in a Bose-Einstein condensate based on micromotion control in a shaken two-dimensional lattice. *Phys. Rev. Lett.* **121**, 030402 (2018).